Ocean Systems Engineering, *Vol. 15, No. 2 (2025) 153-171*
https://doi.org/10.12989/ose.2025.15.2.153

The influence of flow damping on the maritime natural cave performance

Wilson Madaleno Léger Monteiro*[1], António José Nunes de Almeida Sarmento[2], Jakson Augusto Léger Monteiro[1], Bruno Roberto Semedo[1], Arider Barbosa Carvalho[1] and Tomás Tavares Furtado[1]

[1]Faculty of Science and Technology, University of Cabo Verde, P. O. Box: C.P. 379-C, 7943-010, Praia, Cabo Verde
[2]WavEC - Offshore Renewables, Edifício Diogo Cão Doca de Alcântara Norte 1350-352 Lisbon, Portugal

(Received January 4, 2025, Revised May 2, 2025, Accepted May 16, 2025)

Abstract. Maritime Natural Caves (MNCs) are real and natural representations of shoreline Oscillating Water Column (OWC) devices. Recently, one particular MNC located in Cidade Velha on Santiago Island, Cabo Verde, has been the focus of several studies aimed at analyzing its behavior and energy performance under different wave climate conditions. This study investigates the operation of this MNC, focusing on the impact of airflow damping caused by its power take-off mechanism, represented here by orifices (ORs) with different cross-section areas and Wells turbines with various rotor blade stagger angles (β) on its energy extraction and production capacity. Our study showed that the power available from the MNC is linked to the flow damping characterized by the area contraction coefficient and the linear damping coefficient for turbines. The optimum flow contraction coefficient was found to be $C_c = 0.269$, which maximizes both the average and peak power available from the cave, reaching $439.5\,W$ and $4237.9\,W$, respectively. When using turbines, the average power available ranged from 38.3 W to 80.5 W, which was considerably lower than the range observed with orifices (132.2 W – 454.1 W). This suggests that the damping capacity of the turbines could be improved. The turbine with the highest damping coefficient (β=15°) produced the highest values of both available and converted power. However, it showed limitations in effectively converting the energy made available by the MNC. The turbines with moderate damping, between $2.52\,cmH_2O/(m^3/s)$ (turbine with β=0°) and $2.84\,cmH_2O/(m^3/s)$ (β=10°), demonstrated better energy conversion performance with average efficiency of 23.6% and 20.7%, respectively. The remaining turbines exhibited lower average efficiency: 16.6% (β=15°) and 13.3% (β=5°). However, all turbines showed losses of efficiency when the MNC operated with high airflow rates. The turbine with β=0° had a contraction coefficient of 0.545, significantly higher than the optimal found for the orifices. The ideal contraction coefficient could be achieved by increasing both the turbine blades and hub by 60%.

Keywords: airflow damping; maritime natural caves; ocean energy; turbine geometry; wells turbines; orifices damping coefficient

*Corresponding author, Professor, E-mail: wilson.monteiro@docente.unicv.edu.cv

http://www.techno-press.org/?journal=ose&subpage=7 ISSN: 2093-6702 (Print), 2093-677X (Online)

1. Introduction

The performance of an Oscillating Water Column (OWC) device, such as Marine Natural Caves (MNCs), is strongly influenced by several factors, including its geometric characteristics, the properties and compressibility of air, and the damping associated with the turbine coupled to the system.

Humidity and air compressibility are two key properties that significantly impact the performance of an OWC device. For instance, Medina-López *et al*. (2019) demonstrated that humidity can reduce the device's efficiency by approximately 50% to 70% compared to simulations using dry air. Similarly, Moñino *et al*. (2020) found that increasing the water vapour fraction in the air-vapour mixture from 45% to 70% can result in a reduction of approximately 30% in the power available for conversion by the turbine in OWC systems.

Air compressibility is another critical factor in the OWC performance assessment. In addition to contributing to the hysteresis phenomenon, neglecting compressibility can result in an overestimation of system efficiency (Thakker *et al*. 2003). Research by Gonçalves *et al*. (2020) indicates that ignoring air compressibility can result in an overestimation of hydrodynamic performance by approximately 16% to 20%, regardless of whether the system is equipped with a Wells turbine or an impulse turbine.

One of the most important aspects of an OWC system is its integration with the power take-off (PTO) system. Pereiras *et al.* (2015) developed a methodology aimed at identifying the most suitable turbine for a specific OWC configuration. Their approach involved first determining the system's optimal damping and then selecting the turbine that best matched this condition. Bouali *et al*. (2017) explored this issue as well and concluded that, for each OWC device size, there is a unique combination between device dimensions and PTO damping that maximizes energy conversion for a given wave climate.

According to López *et al*. (2014), the hydrodynamic performance of the pneumatic chamber in an OWC device primarily depends on the turbine damping, rather than the wave climate conditions. Therefore, selecting the appropriate turbine for this type of device is crucial, as it impacts both its performance and the chamber's performance, highlighting the importance of the turbine-chamber interaction in such systems. This conclusion is further supported by Bouhrim and Abdellatif (2023), who investigated the flow damping by the air turbine and its relationship to the pneumatic chamber's performance in these devices.

Kamath *et al*. (2015) numerically modelled the damping of the mechanical power generation system in oscillating water column devices. Their research identified a significant correlation between the damping values of the flow created by the mechanical power generation system and the corresponding hydrodynamic efficiency. They found that, as the mechanical system damping increases, the hydrodynamic efficiency initially rises to a peak, before decreasing with further increases in flow damping. Inadequate damping of the device results in the formation of large stagnation zones inside and outside the OWC chamber, which reduces hydrodynamic efficiency. This behavior of OWC devices indicates the existence of an optimal damping value that maximizes the efficiency of their pneumatic chambers.

Nguyen *et al.* (2021) examined how blade pitch angles influence hydrodynamics in a five-bladed vertical-axis hydraulic turbine. By varying the blade pitch angles between -5° and +5°, they found that a +2° pitch angle improved the power coefficient by 2.3%, compared to the value observed at a pitch angle of zero degrees.

Mohamed and Saahaban (2013) studied the effect of blade pitch angles on turbine efficiency,

(a)

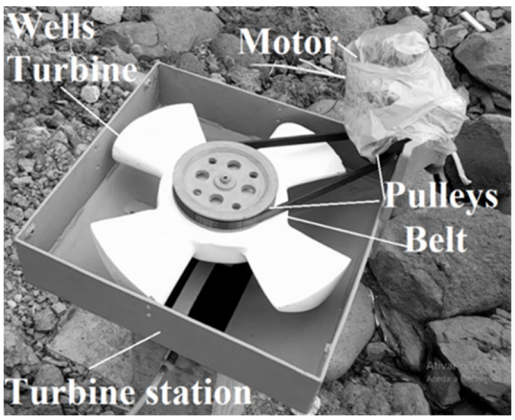

(b)

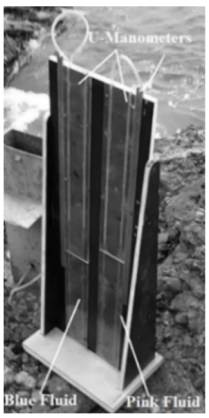

(c)

Fig. 1 (a) Wells turbines with different values of β (one of the turbines was fixed to the turbine operating station)), (b) Turbine workstation and (c) U-manometers

aiming to improve turbine performance through optimized control of these angles. They used two different aerodynamic profiles: the conventional NACA 0021 and an optimized "AOP" profile. Their findings showed an improvement of up to 2.3% for the NACA 0021 profile at a pitch angle of 0.3°, and a substantial improvement of 6.3% for the "AOP" profile.

Gato and Webster (2001) conducted experimental studies on an air turbine with an NACA 0015 profile, achieving efficiency improvements with a 30° back sweep and blade pitch angles ranging from 0° to 20°.

Mohamed and Samehs (2014) achieved improvements of 3.4% in turbine efficiency and 1% in its power at an ideal pitch angle of 0.6°. Thus, the pitch angle not only influences the turbine's performance but also its self-starting capability (Dumitrache *et al*. 2016).

2. Experimental setup and procedure

To measure the performance parameters of the cave equipped with each turbine (Fig. 1(a)), its shaft was connected to the shaft of an electric motor (Fig. 1(b)). Two U-Manometers (Fig. 1(c)) were used to measure the total flow pressure and the static pressure drop across the turbines. The electric motor, which is securely connected to the turbine's operating station, is equipped with a

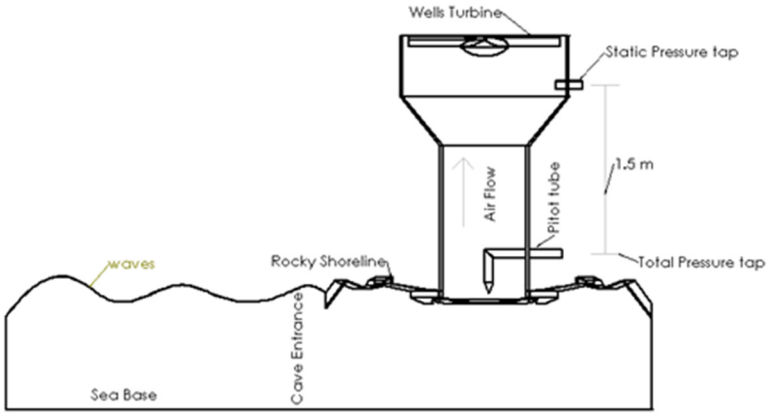

Fig. 2 Sensors arrangements

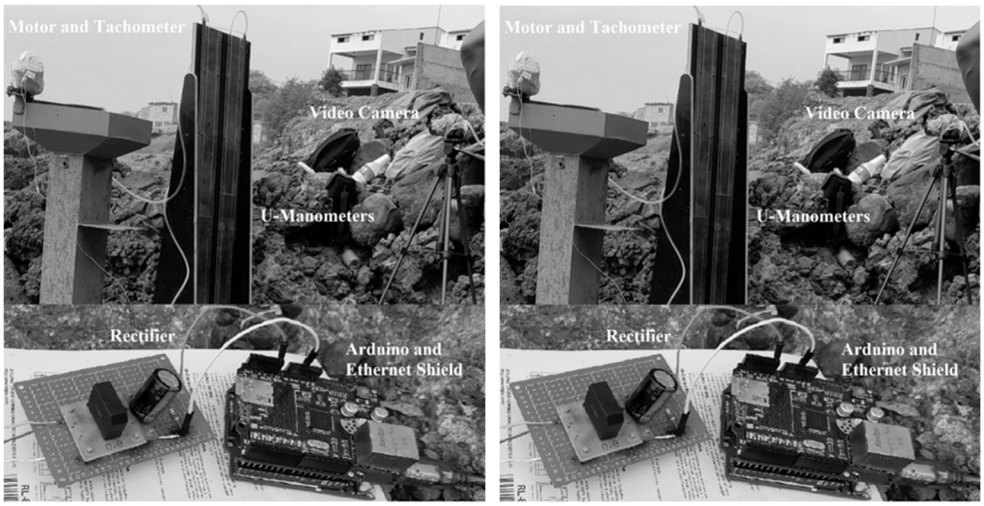

Fig. 3 Experimental Apparatus

tachometer that measures the rotation of its shaft. The belt, shown in Fig. 1(b), transmitted the rotation from the turbine shaft to the motor shaft.

The pressure gauge that measured the total flow pressure had a Pitot tube at one end (Fig. 2) directed into the flow, and the other end was exposed to atmospheric pressure. The pressure gauge that measured the pressure drop across the turbines had one end attached to the side of the vertical duct, perpendicular to the flow, located immediately before the turbines (Fig. 2). The other end was exposed to atmospheric pressure.

The positions of the manometric fluids (pink for total pressure and blue for static pressure) were recorded by a video camera at 25 frames per second and stored on an SD card. The tachometer's voltage signals were captured every 100 ms and converted into the rotation frequency of the motor shaft using a C++ program installed on an Arduino Uno board, which then transmitted these signals to an SD card mounted on an Ethernet shield (Fig. 3). It's important to

Fig. 4 The orifices (ORs) used in this study

note that the AC signals produced by the tachometer were rectified and leveled to a range of 0 to 5 VDC, compatible with the Arduino Uno. All the gathered data were later downloaded to a computer for subsequent analysis.

Fig. 3 displays the experimental setup used to assess the impact of the turbine-damping coefficient on the cave's available and production powers.

To examine the impact of the orifice-damping coefficient on the available power of the MNC, only the pressure gauges were employed to measure both the total flow pressure and the static pressure drop across the orifices (Fig. 4). The instantaneous values of these parameters were captured by the previously mentioned video camera and saved onto an SD card.

3. Methodology

From the instantaneous values of the manometric fluid heights (Δh), the maximum instantaneous velocities (at the tube's axis) were calculated (Eq. (1)). This was done by applying the Bernoulli equation along the central streamline of the tube, assuming incompressible and steady flow for small time intervals (data sampling time).

$$V_{Amax} = \sqrt{\frac{2\rho_{H_2O} g \Delta h}{\rho_{air}}} \tag{1}$$

These values of Δh were measured using U-tube manometers and recorded by a video camera operating at 25 frames per second.

With the values of velocity at the tube's axis and assuming the 1/7 ($n = 7$) turbulent velocity profile law for a circular tube, we calculated the average air velocity in the turbine duct (Eq. (2)) and, therefore, the airflow rate (Q) across the orifices and turbines duct (Eq. (3)).

$$V_A = \frac{2n^2}{(2n+1)(n+1)} \mathrm{V}_{Amax} \quad (2)$$

$$Q = \pi {R_h}^2 V_A \quad (3)$$

In the above equation, R_h is the hydraulic radius of the vertical duct connected to the cave orifice and in which the turbine station was fixed, $a = 30\,cm$ and $b = 15\,cm$ are the dimensions of the cross-section area of this vertical duct.

The average velocity in Eq. (2) was calculated by integrating the previously power law velocity, along the radial direction of the vertical tube (Monteiro *et al.* 2020).

The power available from the cave was determined as the product of the static pressure drop across the orifices and turbines (dp) and the volumetric airflow rate passing through them, using Eq. (4)

$$P_{air} = dpQ \quad (4)$$

The power extracted by the turbine (P) refers to the power at its shaft. This power was calculated by multiplying the turbine torque (M) by its angular velocity (ω), using Eq. (5).

$$P = M\omega \quad (5)$$

In turn, the turbine torque was quantified by multiplying the moment of inertia of the motor-turbine assembly (I) by the turbine angular acceleration (α), through Eq. (6)

$$M = I\alpha \quad (6)$$

The turbine moment of inertia ($I = 145gm^2$) was experimentally estimated in the Lab as explained in the following.

The turbine acceleration was calculated by dividing the change in angular velocity by the data sampling time, which was, in this study, $\Delta t = 0.1s$ (Eq. (7)).

$$\alpha = \Delta\omega/\Delta t \quad (7)$$

The angular velocity of the turbine shaft was derived from the rotational speed of a tachometer shaft connected to it. Voltage signals from the tachometer were converted into turbine angular velocity using a calibration curve established in the lab. This calibration curve was subsequently implemented in Arduino via C++ code, enabling the conversion of electrical signals from the tachometer into the turbine's angular velocity.

To determine the moment of inertia of the turbo-motor assembly, an experimental apparatus was used consisting of two calibrated weights, a ruler, a stopwatch and a wire. The procedure involved inducing rotation in the turbo-motor assembly through the action of a tangential force generated by the vertical fall of a calibrated weight. This weight was connected to the turbine by an inextensible wire, attached tangentially to one of its blades. As the weight fell, it caused the turbo-motor to rotate. The angular velocity of the system was inferred from the tangential velocity at the blade's edge, which corresponds to the slow descent velocity of the falling weight. This tangential velocity was calculated by dividing the vertical displacement of the weight, measured using a ruler, by the time interval recorded with the stopwatch. The angular velocity was then obtained by dividing the tangential velocity by the turbine's radius. Angular acceleration was determined from the change in angular velocity over time, considering the initial angular velocity as zero and the final angular velocity measured at the end of the motion using the stopwatch.

Table 1 Geometric characteristics of Wells turbine (Monteiro *et al.* 2021)

Blade Profile	NACA0021
Solidity	0.72
Tip Radius [mm]	207
h =Hub-to-tip ratio	0.484
Mid Radius [mm]	153
Number of Blades	4
Chord length [mm]	173

Table 2 Tides chart around Santiago Island

Day	1st Tide	2nd Tide		3rd Tide	4th Tide		Coefficient
9 Thursday	0.2 m (2.38h)	1.2 m (8.43h)	$\boldsymbol{\beta = 0°}$	0.2 m (14.37h)	1.3 m (20.57h)	$\boldsymbol{\beta = 0°}$	77 (high)
10 Friday	0.2 m (3.10h)	1.2 m (9.14h)	$\boldsymbol{\beta = 15°}$	0.2m (15.10h)	1.3 m (21.27h)	$\boldsymbol{\beta = 15°}$	71 (high)
11 Saturday	0.2 m (3.42h)	1.1 m (9.48h)	$\boldsymbol{\beta = 10°}$	0.3 m (15.46h)	1.2 m (22.01h)		64(average)
12 Sunday	0.3 m (4.20h)	1.1 m (10.28h)	$\boldsymbol{\beta = 5°}$	0.3 m (16.29h)	1.1 m (22.43h)	$\boldsymbol{\beta = 0°}$	56 (average

The turbine efficiency and the flow coefficient were calculated using Eqs. (8) and (9):

$$\eta^* = \frac{P}{dpQ} \tag{8}$$

$$\varphi = \frac{V_A}{\omega R_{tip}} \tag{9}$$

In the equations above, P and R_{tip} are, respectively, the mechanical power at the turbine shaft and the turbine tip radius.

The Wells turbine used in Cidade-Velha's MNC has four fixed blades staggered at 90° relative to the machine axis, and it was designed to develop 1 kW of shaft power (Monteiro *et al*. 2021). The geometric characteristics of this Wells turbine are presented in the table below.

The turbine involved showed significant energy losses, particularly during high tides when the MNC had the highest energy content (Monteiro *et al.* 2022). Consequently, we aim to analyze the performance of the MNC as a function of the flow-damping coefficient of its mechanical energy conversion system. To achieve this, four turbines were constructed with the same dimensions as those in the previous table, but with varying rotor blade stagger angles to produce different damping coefficients for the device. The blade stagger angle ranged from 0° to 15° in 5° increments, rotated clockwise.

The excitation of the MNC is strongly influenced by tidal conditions and wave characteristics (López *et al*. 2017, Monteiro *et al.* 2021). This made comparing cave performance for different turbines more challenging. However, by analyzing the tide charts for Santiago Island from tabuasdemarés.com, we identified the most suitable scenarios for testing, allowing us to make the comparison as consistent as possible. The following table, extracted from the aforementioned website, provides information on the tidal conditions around Santiago Island during February 2023, the period when the studies were conducted.

As shown in Table 2, there are four tidal states during the day: two low tides (1st and 3rd) and two high tides (2nd and 4th). Each tide is characterized by its height in meters, the day and time it occurs, and its tidal coefficient, expressed as a percentage. This coefficient predicts the tidal amplitude and represents the difference in height between consecutive high and low tides in a given area (tabuasdemarés.com).

To ensure a consistent comparison of cave production with different Wells turbines, tests were conducted under similar tidal conditions. The cave equipped with the β=0° turbine was tested during the second tide on Thursday, February 9, and its performance can be compared with that of the β=15° turbine, tested during the second tide on Friday, February 10. During both tests, the tidal profiles were similar, with a height of 1.2 m and high tidal coefficients. Additionally, the cave with the β=0° turbine (second tide on Sunday, February 12) was compared with the cave using turbines with β=5° (second tide on Sunday, February 12) and β=10° (second tide on Saturday, February 11), as all tests were conducted under similar tidal conditions, characterized by a height of 1.1 m and a mean tidal coefficient.

According to Law-Chune *et al*. (2021), the wave climate changes significantly every 3 hours. As expected, these variations in wave climate impact cave performance. Therefore, the study was carried out during high tides at consistent times to ensure similar wave conditions. Furthermore, data from the website tabuasdemarés.com show only minor variations in significant wave height and wave period, with differences of 0.3 meters and 2 seconds, respectively. These small variations were also verified through on-site observations.

4. Results and discussion

4.1 Error analysis and sources of errors

Before presenting the results of this study, it is essential to address the accuracy of the instruments used in the experimental setup and the propagation of errors in the calculations of the key parameters used to characterize the cave's operation.

To assess the performance of the studied MNC, we measured the total and static air pressures at its outlet using U-tube manometers. Variations in these pressure readings over time were monitored with the aid of graduated rulers. The pressure fluctuations were recorded using a video camera operating at 25 frames per second, corresponding to a temporal resolution of 40 milliseconds.

To calculate the air velocity, we used the formula $V = \left(2\gamma_{H_2O}\Delta h/\rho_{air}\right)^{1/2}$, where $\gamma_{H_2O} = 9810\ N/m^3$ is the specific weight of water, $\rho_{air} = 1.16\ kg/m^3$ is the air density, and Δh is the pressure drop in cmH_2O. The error in velocity measurement due to the use of graduated rulers is given by $dV = K\, d(\Delta h)/\sqrt{\Delta h}$, with $K = \left(\gamma_{H_2O}/2\rho_{air}\right)^{1/2} = 65\ m^{1/2}s^{-1}$ and $d(\Delta h) = 0.5\ mm = 0.5 \times 10^{-3} m$ (typically, the error associated with measurements using rulers is considered to be half of the smallest scale division). In this study, the lowest recorded value of Δh was approximately 0.3 cm. In this worst-case scenario, the associated error in velocity (V) was ±0.6 m/s. For this manometric fluid height, the velocity at the tube axis was calculated to be 7.12 m/s, resulting in a maximum relative error of about 8.2% due to the resolution limit of the measuring scales. Moreover, the uncertainties in Δh readings and velocity calculations led to

estimated errors of around 16.8% in dynamic pressure and 16.6% in static pressure. It is important to emphasize that the Δh values measured under actual operating conditions inside the cave were significantly higher than 0.3 cm, which means the relative errors in those cases were even smaller and can be considered negligible.

The rotational speed of the turbine shaft was measured using a tachometer that had been carefully calibrated in the laboratory. This calibration ensured an accurate relationship between the voltage signal output and the shaft's rotational speed. High-precision instruments were used during the calibration process, including a Fluke digital multimeter (accuracy ranging from 0.5% to 0.025%) and a frequency regulator (maximum accuracy of 0.2%). Therefore, it can be concluded that, in the real case study analyzed, the measurement errors are minimal and do not compromise the evaluation of the cave's performance.

Manometric fluid level measurements (Δh) are subject to potential inaccuracies due to parallax errors. The magnitude of this error depends on the relative positioning of the camera with respect to the free surfaces of the manometric columns, which can vary over time. To improve Δh readings and reduce errors in velocity calculations, the Pitot tube used for measuring maximum velocity at the turbine duct axis should ideally be calibrated in a wind tunnel. Furthermore, the length of the tubing connecting the Pitot probes to the pressure gauges may lead to signal attenuation, potentially masking the true nature of pressure fluctuations and thereby increasing overall data uncertainty.

Another significant source of error stems from the approximation of a rectangular duct as an equivalent circular one using the hydraulic radius. This simplification introduces a degree of inaccuracy in flow parameter estimation. For turbulent flow (Reynolds number $Re > 2300$), the associated error is typically below 12%, depending on the parameter under consideration (Frate *et al*. 2016). However, for laminar flow, the same authors report that relative errors may range from 11% to 23%. Further inaccuracies arise from assumptions made regarding the turbulent velocity profile. The airflow within the duct features two distinct regimes: the entrance region and the fully developed flow region (Oliveira and Lopes 2012). In this study, fully developed turbulence was assumed to estimate the volumetric airflow through the duct cross-section. Nevertheless, since the duct was only 1.5 meters in length, likely, the flow profile had not yet reached the fully developed stage, introducing additional uncertainty into the airflow measurements.

It is also important to acknowledge the inherent difficulty of measuring flows driven by unpredictable events such as coastal sea waves. Selecting instruments capable of adapting to a wide range of unknown flow conditions, while also withstanding the harsh environmental setting in which the measurements were conducted, posed a considerable challenge.

4.2 The influence of orifices flow damping on the MNC performance

We tested the cave using four different orifice restrictors (ORs) to evaluate the influence of their flow-damping characteristics on the MNC's power extraction capability. Each orifice had a distinct flow contraction coefficient (Cc), defined as the ratio between the orifice cross-sectional area (Ao) and the cross-sectional area of the turbine station (As). Therefore, the damping effect of each OR was characterized by its respective flow contraction coefficient. The Cc values for the ORs used in this study were 0.226 (OR 1), 0.338 (OR 2), 0.451 (OR 3), and 0.508 (OR 4).

By fitting each OR to the turbine station, we measured the total airflow pressure and the corresponding static pressure drop across the orifices, focusing solely on the exhaust phase of the cave's operation—when energy production is at its peak.

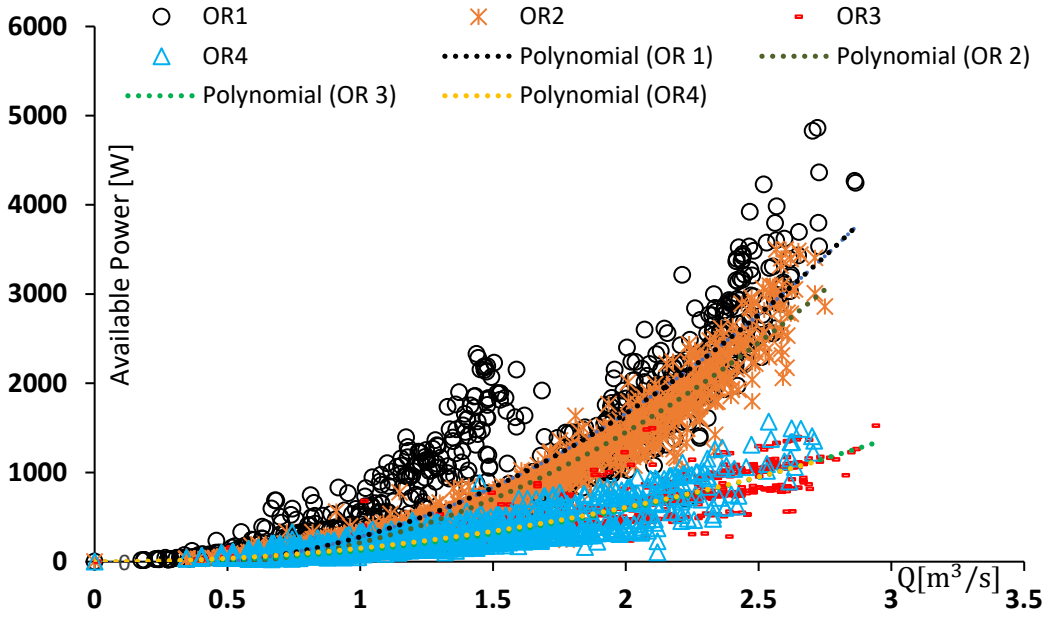

Fig. 5 Cave's available power by each orifice

Fig. 5 presents the available power from the MNC for each OR configuration. Two key observations emerge from these results. First, as anticipated, the relationship between available power and the damping effect of the ORs exhibits a quadratic trend, lending credibility to the experimental setup and methodology. Second, it is clear that different orifice areas (i.e., different damping levels) significantly influence the amount of power the cave can deliver. Notably, OR 1, characterized by the highest flow restriction (smallest passage area), resulted in the greatest available power, suggesting a better match with the cave's operational characteristics compared to the other ORs.

The orifice restrictor (OR) with the lowest airflow restriction (OR 4) yielded the lowest available power from the cave. This result is significant, as it underscores the importance of carefully selecting the power take-off system for converting the cave's available power, given its direct impact on the cave's performance. This finding aligns with the results reported by López *et al.* (2014). Specifically, OR 1 appears to be better suited for both lower (less energetic cave) and higher (more energetic cave) airflow rates, as it consistently provides higher available power compared to the other ORs.

However, it is important to emphasize that although OR 1 demonstrated the best performance among the tested orifices (OR 2, OR 3, and OR 4), this does not necessarily imply that its damping coefficient is the optimal choice for our cave. As highlighted by Kamath *et al.* (2015), there exists an ideal damping coefficient for the power take-off mechanism of an OWC device, where the device's hydrodynamic efficiency is maximized. Therefore, it is important to note that an OR with the ideal damping coefficient has not been tested in this study.

Fig. 6 presents the average and maximum values of the MNC available power as a function of the flow area contraction coefficient ($C_c = A_0/A_s$). The dashed lines represent polynomial approximation curves based on the experimental data. The determination coefficients, R^2 = 0.92

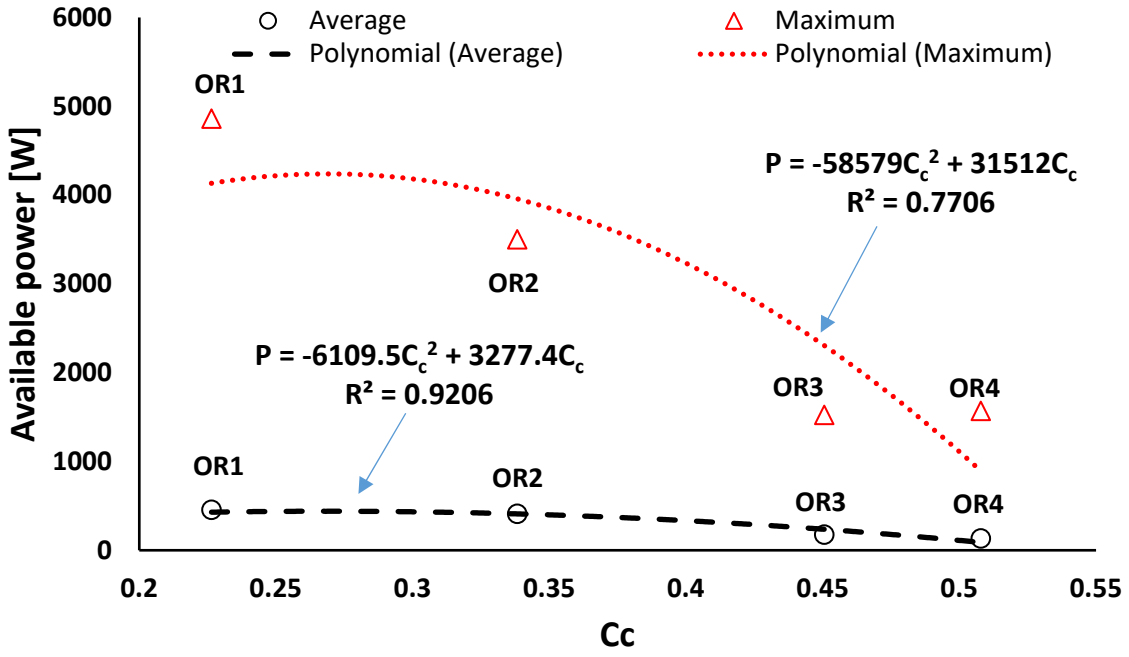

Fig. 6 The MNC available power by each orifice (OR)

for average power and $R^2 = 0.77$ for maximum power, are considered acceptable. These values indicate that the variations in available power can be adequately explained by the variations in the contraction coefficient C_c, as represented by the approximation curves.

Based on the graph under analysis, the approximation curves show downward concavities, suggesting that they have a maximum. Using Excel tools, the equations for the two approximation curves were determined: $P_{air} = -58579C_c^2 + 31512C_c$ (for maximum power) and $P_{air} = -6109.5C_c^2 + 3277.4C_c$ (for average power). From these equations, the optimal flow contraction coefficient that maximizes the MNC's available power was calculated. This corresponds to the value of C_c for which the derivative of power concerning C_c ($dP_{air}/dC_c = 0$) equals zero. By solving this, the optimal C_c value of 0.269 was obtained for both curves. At this ideal C_c value, the highest values of average and maximum available power were 439.5 W and 4237.9 W, respectively.

To achieve these optimal power values, an orifice with a cross-sectional area of 509 cm² would need to be adapted, which is relatively close to the area of OR1. Another noteworthy aspect, shown in Fig. 6, is the significant difference between the average and maximum values of the MNC available power. This discrepancy can be attributed to the large temporal variability in available power, caused by the irregularities and time variations of the waves that excited the MNC.

4.3 The influence of turbine damping on the MNC performance

Fig. 7 shows the characteristic curves of the four turbines tested with the Cidade Velha MNC.

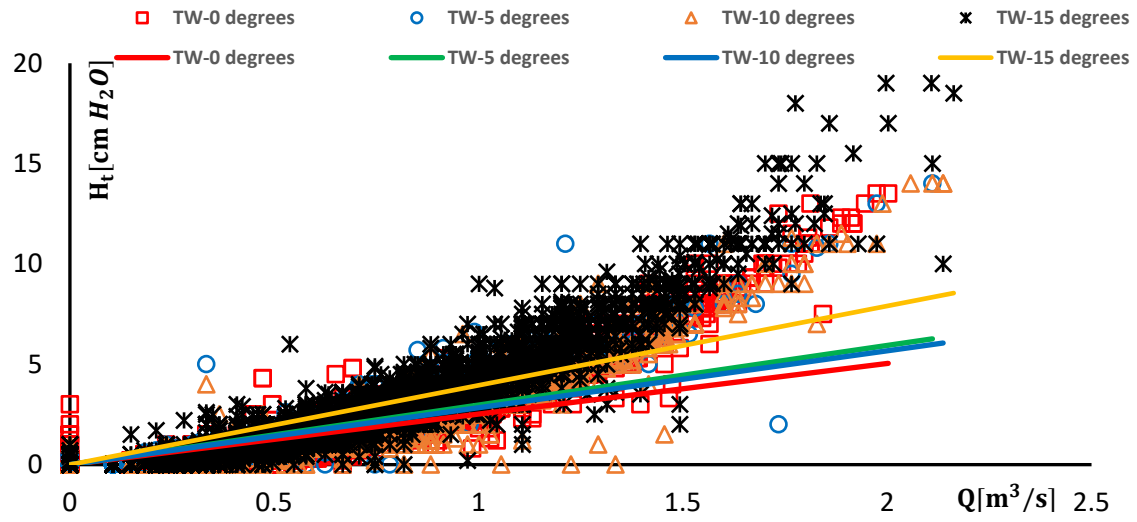

Fig. 7 Characteristic Curves of each Wells turbine

Table 3 Turbine's damping coefficient

Turbines	$\beta = 15°$	$\beta = 10°$	$\beta = 5°$	$\beta = 0°$
K [$cmH_2O/(m^3\ s^{-1})$]	3.95	2.84	2.97	2.52
R^2	0.81	0.73	0.78	0.73

The straight lines are approximations of experimental data through the linear relationship between the manometric height due to the pressure drop across the turbine, $H_t[cmH_2O]$, and the airflow Q that passed through them. The graph shows that the experimental points deviated significantly from the linear approximation curves, especially for high flow values, evidencing non-linearity of the relationship $H_t = f(Q)$. This non-linear behavior of the turbine's characteristics curves is related to the separation of the boundary layer of the airflow over the turbine rotor blades has also been verified by Licheri *et al*. (2023). Apart from this deviation from linearity, the approximation coefficients R^2 are all acceptable, being always higher than 0.73.

From the linear relationship $H_t = KQ$ it was possible to estimate the turbine damping coefficient K shown in the following table.

As shown in Table 3, the K values generally decrease as the blade stagger angle decreases. However, an unexpected behavior was observed between the coefficient values of turbines with β = 10° and β = 5°. This inconsistency is likely related to the imprecision in the data approximation by the linear relationship or possibly due to inaccuracies in our measurements. Regardless, it is important to note that the parameters used to characterize the cave are not affected by this imprecision in the K value.

According to the K values presented in Table 3, the turbine with a β = 15° blade stagger angle exhibited the highest damping coefficient (3.95 $cmH_2O/(m^3\ s^{-1})$), while the turbine with β = 0° had the lowest damping coefficient (2.52 $cmH_2O/(m^3\ s^{-1})$). Additionally, the damping coefficient of the β = 5° turbine was higher than that of the β = 0° turbine. These trends are also reflected in the

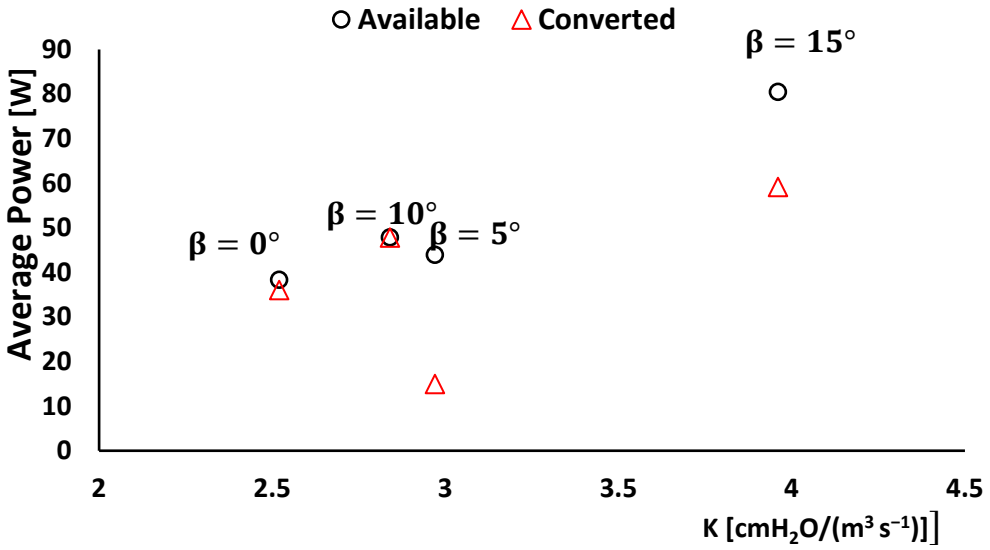

Fig. 8 Cave's available power by each Wells turbine

characteristic curves of the turbines, which showed a decrease in slope as the damping coefficient (K) decreased from β = 15° to β = 0°. Thus, turbines with larger blade stagger angles generated higher pressure drops, meaning they are more effective at damping the flow passing through them. The damping capacity of the turbines plays a direct and significant role in the available and converted powers of the MNC, as illustrated in Fig. 8.

Fig. 8 presents the values of the two aforementioned parameters as a function of the turbine's linear damping coefficients. As outlined in Table 1 in the methodologies section, turbines with 0°, 5°, and 10° blade stagger angles can be compared, as they were tested under similar cave excitation conditions. As shown in Fig. 8, the turbine with the lowest damping coefficient (β = 0°) exhibited lower available and converted power values compared to the turbine with a β = 10° blade stagger angle. The turbine with β = 5° displayed a slight decrease in available power compared to the turbine with β = 0°, but a significant drop in converted power, reaching the lowest value among the turbines tested. This suggests that the turbine with a 5° blade stagger angle experienced the highest aerodynamic losses, likely due to premature flow separation over its blades.

The inability of the turbine with K = 2.97 $cmH_2O/(m^3\ s^{-1})$ (β = 5°) to effectively convert power is further demonstrated in Fig. 9, which compares the power converted by this turbine with that of the turbines with β = 0° and β = 10° as a function of airflow. This figure clearly shows that the power converted by the turbine with β = 5° was significantly lower than that of either the β = 0° or β = 10° turbines.

Returning to Fig. 8, it is important to highlight that, on average, the turbine with a damping coefficient of K = 2.84 $cmH_2O/(m^3\ s^{-1})$ (β = 10°) exhibited the closest values for available and converted powers. This led us to conclude that this turbine was the most efficient at converting available power into shaft power, followed by the turbine with the lowest damping coefficient (β = 0°). In contrast, the turbine with β = 5° showed significant deficiencies in converting pneumatic power into mechanical power.

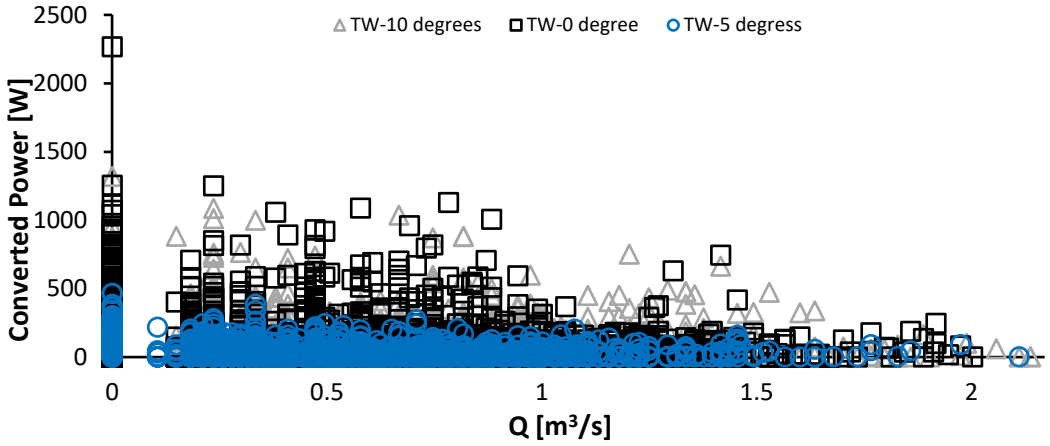

Fig. 9 Turbines converted power

As shown in the same figure (Fig. 8), the turbine with the highest damping coefficient (β = 15°) achieved the highest available and converted powers compared to any of the other turbines tested. However, similar to the turbine with β = 5°, this turbine faced challenges in converting all available power into mechanical power, as its average converted power was significantly lower than its available power. Despite this, the available and converted powers for the turbine with β = 15° surpassed those of any other turbine studied.

4.4 Available power versus converted power

Fig. 10 presents the values of available and converted powers as a function of airflow for the cave equipped with β = 15° turbine blades. The dashed line is the quadratic approximation of the experimental data of the cave's available power. It is important to note that all turbines exhibited similar behaviors to the one shown in the figure. According to this figure, the MNC's available power increased rapidly and continuously with the airflow rate, while the converted power values, although not displaying a well-defined trend, tended to decrease at higher flow rates. As a result, the two curves in Fig. 10 began to diverge, highlighting the losses in turbine efficiency during the period when the cave provided more energy for conversion. This behavior indicates that aerodynamic losses increased significantly at higher flow rates, likely due to the premature separation of the boundary layer over the turbine blades.

As shown in Fig. 10, the turbine exhibited converted power even during the cave's inactivity, when the airflow rate was zero. In these cases, the turbines acted like flywheels, generating shaft power even in the absence of the cave's available power.

4.5 Orifices versus turbines

The following table presents the average power available from the MNC equipped with orifices and turbines. It is evident that the orifice and turbine with the highest available power values are those associated with the highest damping coefficients, namely 454.14 W (OR1) and 80.45 W (turbine with β = 15°). However, the power available from the cave equipped with the orifices

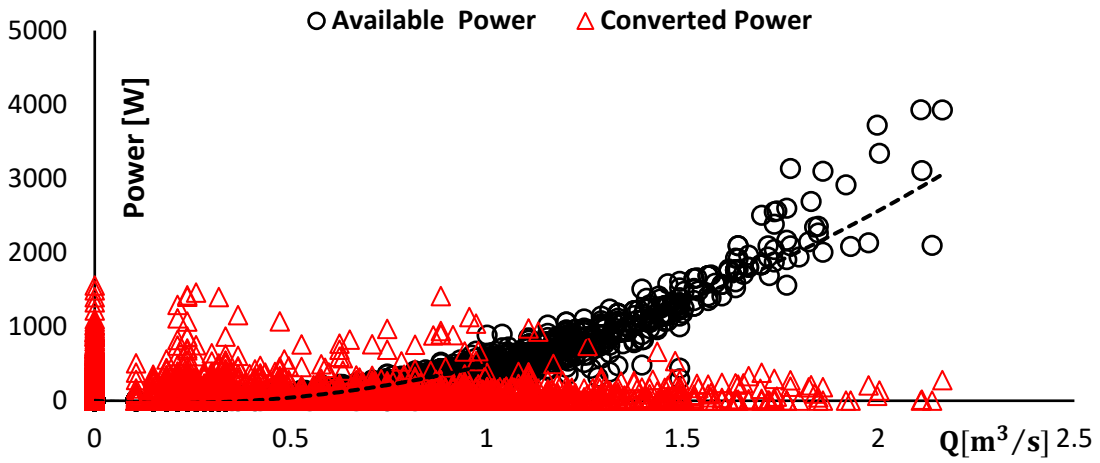

Fig. 10 Available and converted powers for the cave equipped with $\beta = 15°$ rotor blades turbine

(132.15 W–454.14 W) was significantly higher than that obtained with the turbines (38.31 W–80.45 W). The OR4 orifice and the β = 0° blade turbine exhibited the lowest flow damping capacities and, consequently, the lowest available power values, which were 132.15 W (OR4) and 38.31 W (turbine with β = 0°).

Given the cross-sectional area of the β = 0° turbine, which is 864.4 cm², it was possible to determine the contraction coefficient for this turbine, which was found to be 0.545, higher than the optimal value for the orifices (0.269). This difference may help explain, at least partially, the lower available power from the cave equipped with turbines compared to the cave equipped with orifices. To achieve the same ideal contraction coefficient as the orifices, the β = 0° turbine would need to occupy an area of (1 - 0.269) × 1892.25 cm² = 1383.4 cm² in the turbine operation station, which corresponds to a flow area of 509.1 cm². This means the cross-sectional area of the β = 0° turbine would need to be increased by about 60%. This could be achieved by increasing both the blade and wheel hub span by 60%

Therefore, in future work, we plan to construct a larger β = 0° turbine, retest it to assess its performance, and compare it with the turbines already studied.

4.6 Turbine efficiency

The waves that excite the cave are highly irregular and non-linear. As a result, it is common for situations to arise where the cave is excited by a highly energetic wave, followed by a less energetic wave that is unable to alter the energy imparted to the turbine by the previous excitation. This leads to a mismatch between the cave's available power and the power at the turbine shaft, causing significant errors when evaluating the system's performance, resulting in values exceeding 100%. These occurrences were frequent during the MNC operation and are clearly reflected in our data. To address this, by limiting turbine efficiency between zero and one, the average values of this parameter were calculated and are presented in the following table.

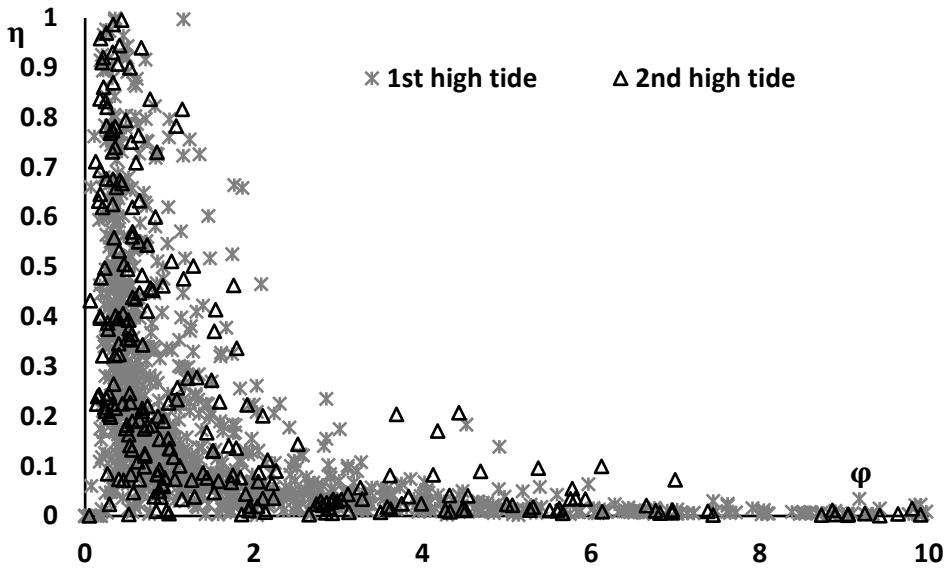

Fig. 11 Turbine Efficiency for $\beta = 15°$ turbine rotor blades

Table 4 Natural Caves' available power

Orifices			
OR1 (Cc =0.226)	**OR2 (0.338)**	**OR3 (0.451)**	**OR4 (0.508)**
454.14 W	409.1 W	175 W	132.15 W
Wells Turbines			
$\boldsymbol{\beta = 15°}$	$\boldsymbol{\beta = 10°}$	$\boldsymbol{\beta = 5°}$	$\boldsymbol{\beta = 0°}$
80.45 W	47.81 W	43.91 W	38.31 W

Table 5 Average values of the turbine efficiencies

Wells Turbines			
$\boldsymbol{\beta = 15°}$	$\boldsymbol{\beta = 10°}$	$\boldsymbol{\beta = 5°}$	$\boldsymbol{\beta = 0°}$
16.6%	20.7%	13.3%	23.6%

The efficiency values presented in this table confirm that the turbine with zero degrees of blade stagger angle was the most efficient, with an efficiency of 23.56%, followed by the turbine with a 10-degree blade stagger angle at 20.7%. The β = 5° turbine proved to be the least efficient among those studied, with an efficiency of 13.26%. The turbine with the highest average converted power exhibited an efficiency of only 16.64%.

It is important to note that the average efficiency values that can be deduced from Fig. 8 are higher than those presented in Table 5. This is because the average powers in Fig. 8 include all values of this parameter, including those associated with efficiency above 100%, while the values shown in Table 5 exclude such extreme efficiency values.

Fig. 11 shows the efficiency of the β = 15° turbine, considering only values of this parameter between 0 and 100%. This figure emphasizes the efficiency losses of the turbine at high airflow rates.

According to Fig. 11, the highest turbine efficiency was achieved for a flow coefficient of approximately 0.33. Beyond this point, there was a rapid decline in efficiency values, highlighting significant efficiency losses. These losses are attributed to the separation of the boundary layer over the turbine blades, a well-documented phenomenon studied in scientific literature (Kinoue *et al*. 2004, Torresi *et al*. 2020, Stefanizzi *et al*. 2023).

4.7 The hysteresis on the cave operation

Another phenomenon that may occur during MNC operation, leading to errors in turbine efficiency assessment, is hysteresis (Morée *et al*. 2020). In this context, Ghisu *et al.* (2020) demonstrated that air compressibility within the pneumatic chamber of the OWC (MNC) device introduces a time delay between the water piston movement and the airflow through the turbine duct. According to these authors, air compressibility is the primary cause of the hysteresis observed in the experimental data of OWC operation. Moreover, their study emphasized that while hysteresis due to turbine aerodynamics is marginal and independent of turbine solidity, hysteresis from air compressibility within the OWC pneumatic chamber is significant and increases with turbine solidity. Consequently, hysteresis will be more pronounced in full-scale OWC plants. Additionally, Puddu *et al.* (2014) noted that hysteresis disappears when turbine performance is presented as a function of flow parameters measured near the turbine rotor. In our setup, the pressure sensors were positioned along the vertical duct, relatively close to the turbine rotor. Therefore, we believe that hysteresis due to air compressibility was negligible in our data. However, since the two sensors were positioned 1.5 m apart, this could have introduced some lag between their responses, causing time delays between the values recorded by them, creating an effect similar to hysteresis caused by air compressibility.

5. Conclusions

The current study used a set of orifices to simulate air turbines and assessed how flow damping, due to the flow contraction coefficient, of these models influenced the cave's available power. These power values were then compared to those generated by four real Wells turbines, each with a different blade stagger angle, resulting in varying turbine damping coefficients. The orifice with the highest damping coefficient (OR1) produced the highest available power values. By analyzing the experimental data, we calculated the optimal flow contraction coefficient ($C_c = 0.269$) that maximizes the cave's power potential.

The turbine with the highest damping coefficient (β=15°) exhibited the highest available and converted powers, but faced challenges in converting a significant portion of the power provided by the cave. The results show that the turbine with β=0° was the most efficient, achieving an average efficiency of 23.6%, followed by the turbine with β=10°, which reached 20.7%. The turbine with β=5° was the least efficient, with an average efficiency of just 13.26%. Meanwhile, the turbine associated with the highest values of available and converted power achieved an efficiency of 16.6%.

In general, all turbines struggled to convert energy when the cave presented higher energy

content. The power available in the cave equipped with turbines was significantly lower than that obtained with the orifices. This discrepancy led to the conclusion that the turbines' damping coefficients were not ideal for the MNC operation. Specifically, for the turbine with β=0°, we determined the contraction coefficient to be 0.544—much higher than the optimal value of 0.269 derived from the orifice tests. According to the findings, to match the optimal contraction coefficient, the turbine would need to increase in size by 60%.

Acknowledgements

Special thanks go to our Ministry of Education, United Nations Development Programme (PNUD) and to Nivaldo Da Veiga Moreira, a mechanical engineering student at the University of Cabo Verde, for their valuable contribution to this study.

References

Bouali, B. and Larbi, S. (2017), "Sequential optimization and performance prediction of an oscillating water column wave energy converter", *Ocean Eng.*, **131**, 162-173. https://doi.org/10.1016/j.oceaneng.2017.01.004.

Bouhrim, H. and Abdellatif, E.M. (2023), "Effects of turbine damping and wave condition on OWC performances for optimal wave energy conversion", *J. Ocean Eng. Mar. Energ.*, https://doi.org/10.1007/s40722-023-00293-y.

Dumitrache, A., Frunzulica, F., Dumitresco, H. and Suatean, B. (2016), "Influences of some parameters on the performance of a small vertical axis wind turbine", *Renew. Energ. Environ. Sustain.*, **1**, 16. https://doi.org/10.1051/rees/2016024.

Frate, L., Moretti,F., Galassi, G. and D'Auria, F. (2016), "Limitations in the use of the equivalent diameter", published by World J. Nuclear Sci. Technol., **6**(1). https://doi.org/10.4236/wjnst.2016.61005.

Gato, L.M.C. and Webster, M. (2015), "An experimental investigation into the effect of rotor blade sweep on the performance of the variable-pitch wells turbine", *Proc. Inst. Mech. Eng., Part A J. Power Energ.*, **215**(5), https://doi.org/10.1243/0957650011538848.

Ghisu, T., Cambuli, F., Puddu, P., Virdis, I. and Carta, M. (2020), "A lumped parameter model to explain the cause of hysteresis in OWC-Wells turbine systems for wave energy conversion", *Appl. Ocean Res.*, **94**, 101994. https://doi.org/10.1016/j.apor.2019101994.

Goncalves, R.A.A.C., Teixeira, P.R.F., Didier, E. and Torres, F.R. (2020), "Numerical analysis of the influence of air compressibility effects on an oscillating water column wave energy converter chamber", *Renew. Energ.*, **153**, 1183-1193. https://doi.org/10.1016/j.renene.2020.02.080.

Kamath, A., Bihs, H. and Arntsen, O.A. (2015), "Numerical modeling of power take-off damping in an OWC device", *Int. J. Mar. Energ.*, **10**, 1-16. https://doi.org/10.1016/j.ijome.2015.01.001.

Kinoue, Y., Setoguchi, T., Kim, T.H., Mamun, M., Kaneko, K. and Inoue, M. (2004), "Hysteretic characteristics of the Wells turbine in a deep stall condition", *Proc. Inst. Mech. Eng. Part M.*, **218**(3), 167-173. https://doi.org/10.1243/1475090041737967.

Law-Chune, S., Aouf, Alice, L.D., Levier, B., Drillet, Y. and Drevillon, M. (2021), "WAVERYS: A CMEMS global wave reanalysis during the altimetry period", *Ocean Dynam.*, **71**(3). https://doi.org/10.1007/s10236-020-01433-w, 2021.

López, I., Pereiras, B., Castro, F. and Iglesias, G. (2017), "Performance of OWC wave energy converters: influence of turbine damping and tidal variability", *Int. J. Energ. Res.*, **39**(4), 472-483. https://doi.org/10.1002/er.3239.

Licheri, F., Ghisu, T., Cambuli, F. and Puddu, P. (2023), "Experimental characterization of a variable-pitch Wells turbine", *J. Phys. Conf. Series*, **2891**(1), 01213. https://doi.org/10.1088/1742-6596/2893/1/012131.

Torresi, M., Stefanizzi, M.M., Gurnari, L., Filianoti, F. and Camporeale, T.M. (2020), "Experimental characterization of the unsteady performance behavior of a Wells turbine operating at high flow rate coefficients", *Proc. Web of Conferences*, **197**, 08009. https://doi.org/10.1051/e3sconf/202019708009.

Medina-Lopez, E., Borthwick, A.G.L. and Moñino, A. (2019), "Analytical and numerical simulations of an oscillating water column with humidity in the air chamber", *J. Clean. Prod*., **238**, 117898. https://doi.org/10.1016/j.jclepro.2019.117898.

Mohamed, M.H. and Samehs, S. (2014), "Numerical optimization of axial turbine with self-pitch-controlled blade used for wave energy conversion", *Int. J. Energ. Res*., **38**, 592-601. https://doi.org/10.1002/er.3064.

Mohamed, M.H. and Shaaban, S. (2013), "Optimization of blade pitch angle of an axial turbine used for wave energy conversion", *Energy*, **56**, 229-239. https://doi.org/10.1016/j.energy.2013.04.035.

Moñino, A., Quirós, C., Mengíbar, F., Medina-Lopez, E. and Clavero, M. (2020), "Thermodynamics of the OWC chamber: Experimental turbine performance under stationary flow", *Renew. Energ*., **155**, 317-329. https://doi.org/10.1016/j.renene.2020.03.141.

Monteiro, W.M.L., Sarmento, A., Monteiro, C.P. and Monteiro, J.A.L. (2021), "Wave energy production by a maritime Natural Cave: Performance characterization and the power take-off design", *J. Ocean Eng. Mar. Energ.*, **7**, 327-337. https://doi.org/10.1007/s40722-021-00196 w.

Monteiro, W.M.L., Sarmento, A., Monteiro, J.A.L. and Monteiro, C.P. (2022), "Wave energy production by a maritime natural cave equipped with Wells turbine", *J. Ocean Eng. Mar. Energ*., **8**, 457-467. https://doi.org/10.1007/s40722-022-00234-1.

Mörée, G. and Leijon, M. (2023), "Review of hysteresis models for magnetic materials", *Energies*, **16**, 3908. https://doi.org/10.3390/en16093908.

Nguyen, M.T., Balduzzi, F. and Goude, A. (2021), "Effect of pitch angle on power and hydrodynamics of a vertical axis turbine", *Ocean Eng*., **238**, 109335. https://doi.org/10.1016/j.oceaneng.2021.109335.

Oliveira, L. and Lopes, A. (2012), Mecânica dos Fluidos", 4ª Ed., Lidel.

Pereiras, B., Lopez, I., Castro, F. and Iglesias, G. (2015), "Non-dimensional analysis for matching an impulse turbine to an OWC (oscillating water column) with an optimum energy transfer", *Energy*, **87**, 481-489. https://doi.org/10.1016/j.energy.2015.05.018.

Puddu, P., Paderi, M. and Manca, C. (2014), "Aerodynamic characterization of a Wells turbine under bi-directional airflow", *Energy Procediam*, **45**, 278-287. https://doi.org/10.1016/j.egypro.2014.01.030.

Stefanizzi, M., Camporeale, S.M. and Torresi, M. (2023), "Experimental investigation of a Wells turbine under dynamic stall conditions for wave energy conversion", *Renew. Energ*., **214**, 369-382. https://doi.org/10.1016/j.renene.2023.05.120

MK